Chapter 4

Energy absorption in C_{60} : Rydberg Series

Photoelectron spectra of C_{60} measured after the interaction with femtosecond laser radiation have exhibited a rich structure. An initial interpretation of Rydberg states has been proposed in [BHS01]. In the context of this work, this peaked structure was to be experimentally investigated to better understand the population and ionization mechanisms and dynamics. A series of experimental measurements on Rydberg series of C_{60} is presented in this chapter. These experiments have led to a better understanding of these states and new interpretations of their population.

4.1 Introduction to Rydberg Series

The term "Rydberg series" refers to the series of bound electronic states of constant angular momentum and varying principle quantum number. The progression of states is described by the equation 4.1.

$$E_n = IP - \frac{R}{(n-\delta)^2} \tag{4.1}$$

where R is the Rydberg constant 13.6 eV, n is the principle quantum number, and δ is the quantum defect. Since the binding energy is dependent on the angular momentum quantum number, a different series exists for each ℓ. As n increases, the energy level spacings become smaller as they approach the ionization potential.

The quantum defect is the measurement of the deviation of electronic motion from a purely Coulombic point charge interaction, in other words this quantity is

the deviation from Hydrogenic nature. The quantum defect is angular momentum dependent, as it reflects the electronic wavefunction overlap with the core. For atoms, the quantum defect is highest for $\ell = 0$ and decreases with increasing ℓ.

Several molecules have also exhibited Rydberg series structure, for example, phenol [SWe01a] and benzene and toluene [WGr83]. For a general overview of higher excited states of polyatomic molecules, see [Rob75a]. A molecular Rydberg state can be defined as a state when one electron has become highly excited so that the orbital radius is much larger than the core, hence the core can be treated as a point charge.

4.1.1 Rydberg Series of C_{60} : Previous Results

Initial photoelectron spectra of C_{60} measured with femtosecond laser pulses of moderate intensities exhibit a rich structure. A complete review of the first measurements can be found in the thesis of Hoffmann [Hof00], which focuses on a series of measurements performed at the Quantronix Laser System which comprises the narrowest energy bandwidth (10 meV) of all the ultrafast systems used for excitation of C_{60} in the present work. A first interpretation of the observed photoelectron structure was also presented, but is now thought to be incorrect. A brief summary will be presented in this section.

The laser intensity dependence of the photoelectron spectra, show for low laser intensities (10^{12} W/cm^2) numerous peaks emerging from the broad thermal background. These spectra were taken with a central wavelength of 800 nm with a chirped pulse duration of 1.5 ps. The resonance peaks are most apparent at the weakest intensity shown, 1.1*10^{12} W/cm^2. These peaks are seen to be only a small part of the entire spectra, indicating that the electronic states they correspond to are not easily excited. The broad thermal background is understood to be statistical electron emission from a hot electronic system [HHC03][CHH00].

These peaks were found to be highly reproducible even under different laser conditions including intensity (or fluence) and pulse duration. The spectrum with the most resolved peaks was taken with a pulse duration of 1.5 ps (but an energy bandwidth of 10meV) .

Fig. 4.1 presents a photoelectron kinetic energy distribution of C_{60} between 0 and 2 eV and the first analysis of the structure as Rydberg series. No obvious equivalent spacing of the peaks can be determined, which indicates that they do not form a vibrational progression. The first interpretation of these lines was Rydberg series, as

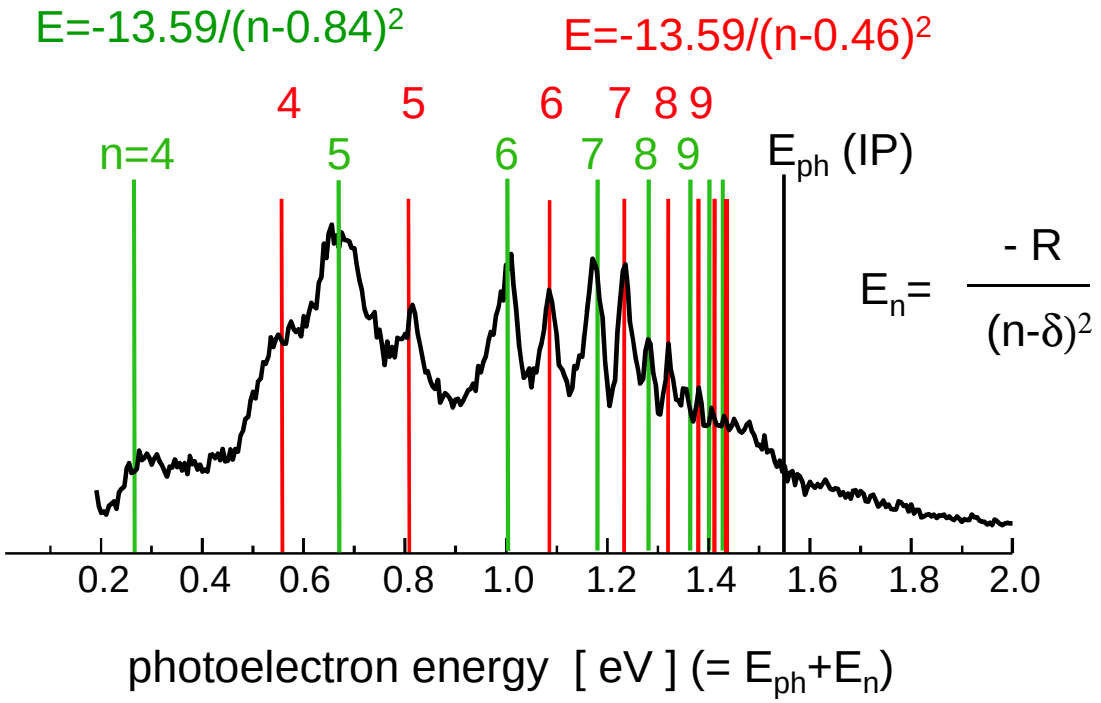

Figure 4.1: *Photoelectron spectrum of C_{60} with first analysis of resonance peaks. Two Rydberg series were found with quantum defects of δ= 0.84 and 0.46(adapted from [Hof00]). The photoelectron spectrum was taken with a 800 nm, 1.5 ps, 8.6 * 10^{11} W/cm^2 laser pulse.*

the peaks converged as their kinetic energy increases to 1 photon above the ionization potential.

The spectrum shown was obtained with a pulse duration of 1.5 ps with 8.6*10^{11} W/cm^2, and at a central wavelength of 800 nm. Superimposed are two series as a function of the principle quantum number, n, as in the equation 4.1. Two quantum defects were determined, δ = 0.84 and 0.46. Although the electronic peak positions fit well to a Rydberg Series [Hof00], the principle quantum number was empirically chosen.

Photoelectron emission was also measured using the second harmonic (400 nm) as the excitation source. A number of peaks were again observed on top of the thermal background [Hof00]. Similar intensity and pulse duration dependencies were found for this shorter wavelength. Fig. 4.2 shows the photoelectron spectrum resulting from 400 nm excitation of 1.4 ps pulse duration and an intensity of 4.4*10^{10} W/cm^2 and shows Lorentzian peak fits and thermal electron distribution at T = 8000 K.

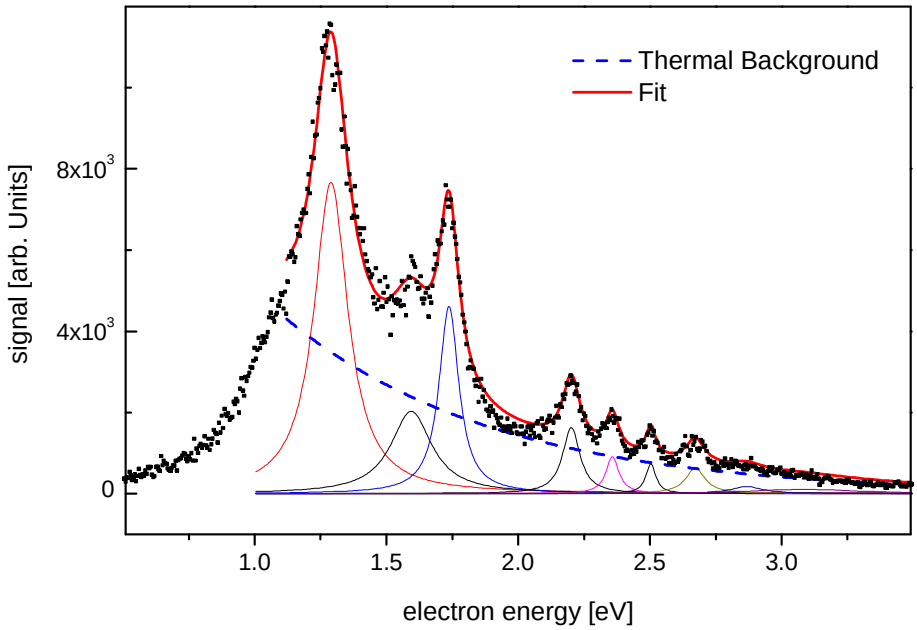

Figure 4.2: *Photoelectron spectrum of C_{60} resulting from 400nm excitation. Experimental data (symbols) with a sum of Lorentzian peak fits and the calculated thermal electron distribution (solid line). The thermal background is indicated by the dashed line.(adapted from [Hof00].)*

The interpretation of the electronic structure observed in photoelectron spectra of 800 nm and 400 nm was different for the two wavelengths. The interpretation is now considered to be incorrect and has been the focus of this thesis.

4.2 Experimental Observations and Discussion

This work has expanded on the understanding of the observed peaks, identifying their electronic nature, labelling the states, as well as developing an excitation mechanism. In the first section, results from a series of single pulse measurements will be presented. The second section provides information about modelling of the electronic structure followed by a hypothesis for excitation of these states in section three. The fourth and fifth section will present experiments which tested the excitation hypothesis. These sections present results of two-color time-resolved pump-probe measurements and the role of internal energy, respectively. These two experiments have led to a new interpretation of the excitation mechanism, which will be presented in section six.

Finally, the first coincident angular resolved photoelectron images will be presented with specific focus on electronic energies corresponding with the Rydberg series.

4.2.1 Single Pulse Laser Excitation

A series of experiments were performed with single pulse measurements to gain further insight into the population and ionization of the observed structure. By varying the polarization axis of the incident linearly polarized laser radiation, the chirp, the energy bandwidth, and the wavelength, important information was gained about the ionization related to the structure [BHS02].

First, the electron emission mechanism was investigated. By rotating the polarization we can distinguish between direct and statistical emission processes. Direct emission processes occur during the laser pulse. The angular distribution for C_{60} is known to be primarily oriented along the laser polarization axis [Hof00]. A statistical emission process occurs after electronic energy redistribution, after the laser pulse no longer interacts with the molecule. An isotropic distribution is expected.

Typically, the laser polarization is oriented along the TOF axis (horizontally polarized), since the total electron yield is peaked along this axis. A comparison of photoelectron spectra measured with horizontal and vertical polarization (the latter being perpendicular to the TOF axis) light is presented in Fig. 4.3. These spectra were taken with bandwidth limited pulse durations (180 fs) at 800 nm and an intensity of $\sim 5{*}10^{12}$ W/cm^2. The trace with larger signal at 1 eV represents the photoelectron spectrum taken with polarization parallel to the TOF axis. This was the typical orientation for the previous photoelectron experiments. The presence of four peaks between 1.0 and 1.2 eV is observed and are consistent with previous measurements. The resolution of the spectra is worse than that of Fig. 4.1, but comparable to the spectrum measured with 180 fs in [Hof00].

The photoelectron spectrum for laser polarization perpendicular to the TOF axis is given by the black line. A suppression of the four peaks between 1.0 and 1.2 eV is observed, while the prominent peak at 0.4 eV has a similar intensity. Thus, the photoelectron angular distribution (PAD) of these four peaks is not isotropic, although it should be noted that the peaks are not completely suppressed. An anisotropic distribution indicates that these electrons are not emitted through statistical electron emission, but rather in a direct process during the laser irradiation. Further information about the PAD of C_{60} will be given in a later section of this chapter.

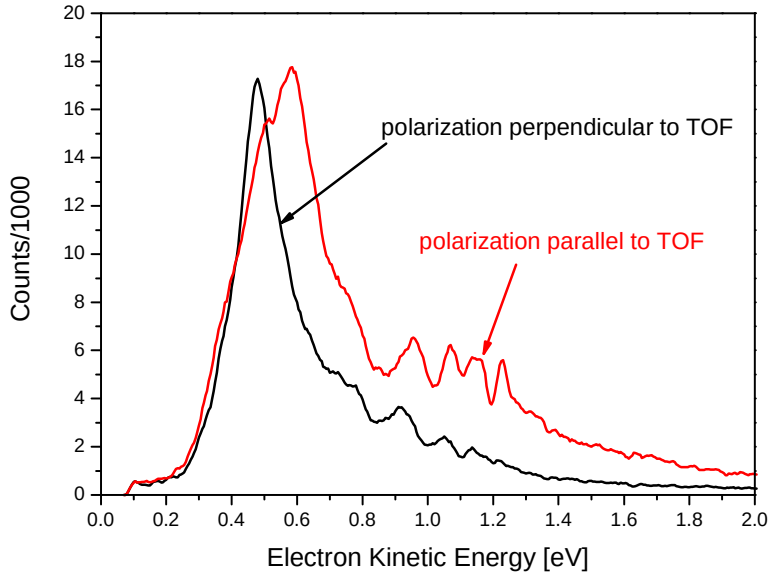

Figure 4.3: *Polarization dependence on the photoelectron spectrum of C_{60} . Spectra recorded with bandwidth limited pulse durations of 180 fs at central wavelength 800 nm and an intensity of 5*10^{12} W/cm^2.*

Further evidence of a direct emission process can be inferred from the photoelectron spectrum dependence on the chirp of the laser radiation. Positive and negative chirp can be introduced by changing the position of the output compressor grating of a CPA. Although the energy bandwidth remains the same, the chirp (both positive and negative) increases the pulse duration from the bandwidth limited value. In Fig. 4.4, photoelectron spectra from a positively and negatively chirped pulses are compared. The plot compares the electron yield versus the kinetic energy, as calculated from the time-of-flight measurement.

These spectra were taken under similar laser condition (800 nm, 1.5 ps, and 2*10^{12} W/cm^2) except that the chirp was reversed. The spectrum with positive chirp (when red frequencies leads blue frequencies) is shifted by 10 meV with respect to the negatively chirped laser pulse. This shift is equivalent to the laser energy bandwidth. This is interpreted to be the leading portion of the pulse populating the excited electronic states and the trailing portion of the pulse ionizing from these states. This is consistent with the picture that the electrons are emitted during the laser pulse duration.

A comparison of the photoelectron spectra measured with different pulse durations, as seen in Fig. 4.5, shows that for decreasing pulse duration (increasing energy

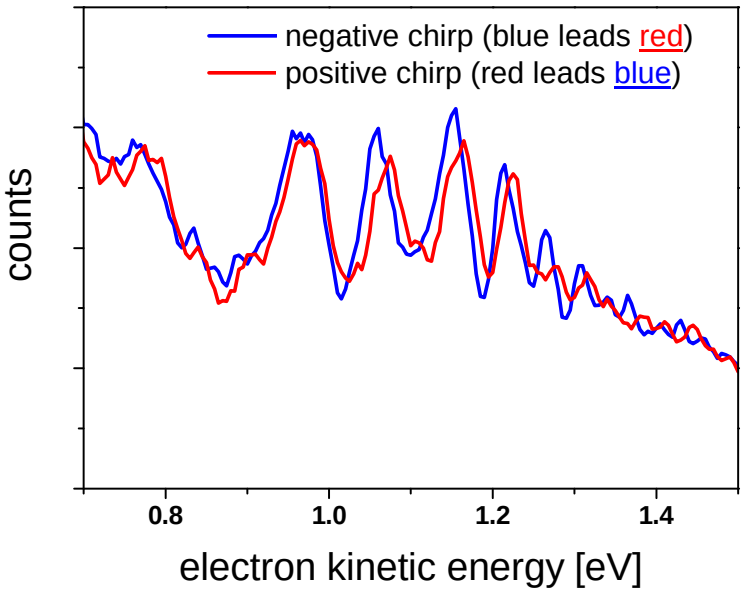

Figure 4.4: *Chirp dependence on the photoelectron spectrum of C_{60} . The laser pulse duration was ∼ 1.5 ps (not energy bandwidth limited) for both cases. The energy bandwidth of the laser was 10 meV and supports a minimal pulse duration of 180 fs.*

bandwidth) the resolution of the peaks decreases. Each plot displays the photoelectron yield versus kinetic energy. The decrease in resolution is expected when the laser energy bandwidth is large in comparison to the energy bandwidth of the state, since the measured energy bandwidth, $\Delta E_{measured}$, is equal to the convolution of laser energy bandwidth and the energy line width due to the lifetime of the state.

$$\Delta E_{measured} = \Delta E_{laser} \times \Delta E_{lifetime} \tag{4.2}$$

Hoffmann has demonstrated that the measured spectrum at 20 meV energy bandwidth agrees well with the spectrum measured at 10 meV, when accounting for the wider energy bandwidth of the laser [Hof00]. A spectrum from an 85 meV energy bandwidth laser (e.g. 30 fs pulse duration), also demonstrates a broad (unresolved) peak at the appropriate kinetic energy value. Although not discussed explicitly in the Hoffmann thesis, it is obvious that the Rydberg states must be able to be produced and ionized on a timescale as short as 30 fs.

Also, the measured line widths of the higher lying Rydberg states are on the order of the laser energy bandwidth, which indicates that the natural line width of these states are significantly narrower and thus indicates that the upper limit of the lifetime

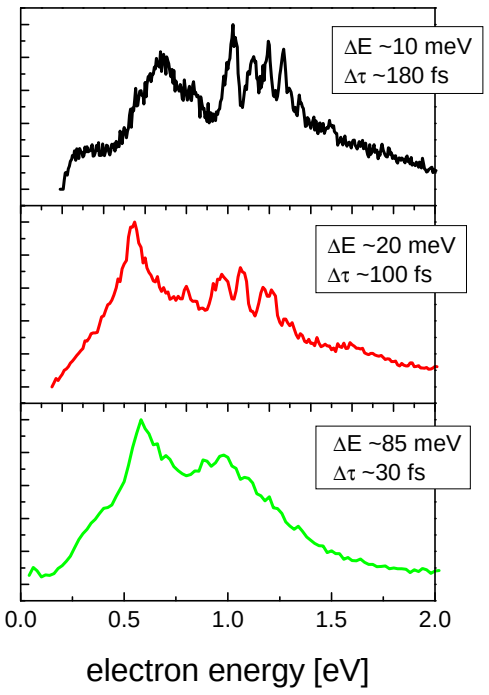

Figure 4.5: *Energy bandwidth dependence on the photoelectron spectrum of C_{60} , the broader energy bandwidth causes the decrease in measured resolution.*

is on the order of hundreds of fs. The lifetime scales as n^3 for atoms, however, for molecules the lifetime is limited by collisions with the significantly larger core. The lifetimes are expected to increase for larger n (of a particular angular momentum) since the radius will be larger and will have a longer orbital period. The recurrence time of the low lying Rydberg states is expected to be on the order of 10-100fs [CLe00]. The experimental upper limit of the lifetime indicates that the excited electron will orbit twice before interacting with the core and either the electron is emitted or it couples to the valence electronic states.

Plotting the photoelectron signal versus the binding energy allows a direct comparison of the populated states lying below the ionization potential after excitation with different photon energy sources. The binding energy (BE) is calculated from the relation BE = hν - KE, where KE is the measured kinetic energy. This assumes that an electron is emitted through ionization by one photon. Fig. 4.6 shows such photoelectron spectra of 800 nm, 660 nm, and 400 nm excitation. Both 800 nm and 400 nm spectra were measured at the optimal pulse duration for the best resolution of the peaks. The 660 nm was measured at a much shorter duration since the con-

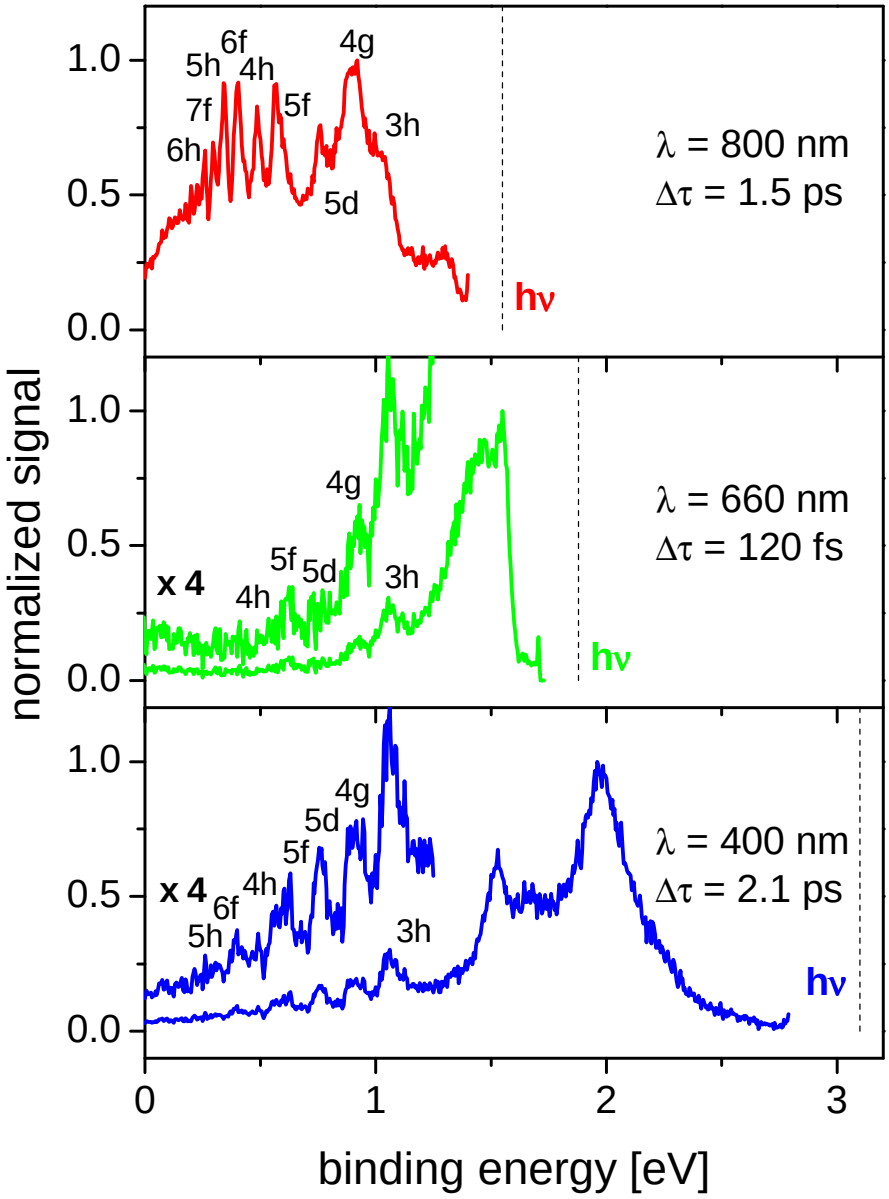

Figure 4.6: *Wavelength dependence of the photoelectron spectrum of C_{60} . The measured kinetic energy spectra plotted against binding energy illuminates the similarity.*

version efficiency in the OPA allowed for barely enough energy per pulse (directly proportional to intensity) to ionize C_{60} . All three wavelengths display states of the same binding energy, although their relative yield is not comparable.

The measured binding energy can be attributed to certain (nℓ) electronic states, as will be shown in the following section. The excitation of these states appear to be wavelength independent. Surprising since a different number of photons are needed to populate these states (4 hν of 800 nm, 3 hν of 660 nm, and 2 hν of 400 nm). This indicates that a broad intermediate state is needed for population.

In summary, the single pulse measurements indicate:

1.) the population of the Rydberg states and ionization process occur during the same laser pulse

2.) these two processes must be extremely fast ($<$ 30 fs)

3.) population occurs at the beginning part of the laser pulse and electron emission from the latter portion

4.) ionization of the Rydberg states occurs through a direct one photon absorption process

5.) population is wavelength independent.

The series of measurements with single pulse excitation have elucidated the electron emission (ionization) process of C_{60} , as is shown in the next section these peaks can be identified through a quantitative analysis. However, these series of measurements have provided at best cryptic clues as to their population, further experiments will be described in the following sections.

4.2.2 Calculation of Binding Energies

To quantitatively understand the peak structure, the binding energies of excited electronic states were calculated. The Schrödinger equation was analytically solved for the binding energies of single electrons orbiting in a spherically symmetric potential. The Mathematica program used to solve this problem was provided by F. Schöberl [FGS85, LSc99] and was tested with the binding energies of Hydrogen[1].

The Schrödinger equation was solved with the Runge-Kutta method and can be

[1]In the Mathematica calculation, "n" represents the number of nodes in the radial wavefunction. This must be converted to the jellium notation by $n_{jellium}$ = "n" + 1. To avoid confusion, the number of nodes will be called N in the text.

written as

$$\left[\frac{\hbar^2}{2\mu}\left(-\frac{d^2}{dr^2}+\frac{\ell\,(\ell+1)}{r^2}\right)+V_0(r)\right]\psi_{N,\ell}(r)=E_{N,\ell}\psi_{N,\ell}(r) \tag{4.3}$$

where $\ell = 0, 1, 2, ...$ denotes the angular momentum quantum number, μ the reduced mass, V_0 is a spherically symmetric potential of C_{60}, and $E_{N,\ell}$ is the energy eigenvalue, with $N = 0, 1, 2, ...$ indicating the number of nodes. In the jellium notation, the number of nodes is one less than the number $n_{jellium}$, i.e., $N = n_{jellium} - 1)$.

The potential used in the calculation was adapted from [PNi93] and is based on the jellium model, in which the electrons move freely, so that the positive charge can be considered homogenously distributed. This model is justified for C_{60} because the location of the carbon atoms is symmetric with respect to the radius and the 60 delocalized π-electrons. The jellium model has been successfully employed in several theoretical studies on C_{60} [PNi93, FRo97, RHB02].

The C_{60} system can be on a first or approximation represented as a hollow, polarizable sphere. The spherically symmetric model potential is shown in Fig. 4.7a as a one dimensional curve of the potential energy plotted against the radius. The deep well represents the cage wall, where 240 valence electrons are present (180 σ electrons, 60 π electrons). The center of the well is located at 6.7 a.u. (3.35 $\mathring{A}$) [PNi93]. The potential outside the cage is a 1/r Coulomb potential, the singly charged C_{60} can be considered as a point charge. Inside the sphere, the electronic potential decreases to approximately zero at the center of the cage and thus does not model a perfectly conducting sphere. The potential is mathematically shown in Eq. 4.4.

$$V_0(r)=\begin{cases} -2e^{-6.69\,|r-6.69|}-\frac{1}{|r-6.69|} & \text{if} \quad r<5.13 \\ \frac{-1.5}{1+e^{\frac{|r-6.69|-1.558}{0.006}}} & \text{if} \quad 5.13\le r<5.15 \\ 0.012(6.69-r)^4-1.50 & \text{if} \quad 5.15\le r\le 8.23 \\ \frac{-1.5}{1+e^{\frac{|r-6.69|-1.558}{0.006}}} & \text{if} \quad 8.23<r\le 8.25 \\ -2e^{-6.69\,|r-6.69|}-\frac{1}{|r-6.69|} & \text{if} \quad 8.25<r \end{cases} \tag{4.4}$$

It should be noted that the notation of electronic states given in this section correspond to the notation used in jellium models; $n_{jellium}$ is equal to the number of radial modes plus one ($n_{jellium} = N + 1$) in the electronic wavefunction and not the principle quantum number associated with Bohr type orbitals, and ℓ is the angular momentum quantum number. The binding energies were calculated for several angular momentum states, $\ell = 0$ to 7, for different $n_{jellium}$. The results are shown in

Fig. 4.7b. The series are plotted as a function of $1/\sqrt{BE}$. The binding energy found for the highest occupied molecular orbital (HOMO) ($n_{jellium}$=2, ℓ=5) was 7.58 eV, in good agreement with the experimentally measured ionization potential of 7.59 eV ± 0.02 eV [SHH95]. Additional binding energies were checked and were found to be in agreement with [PNi93].

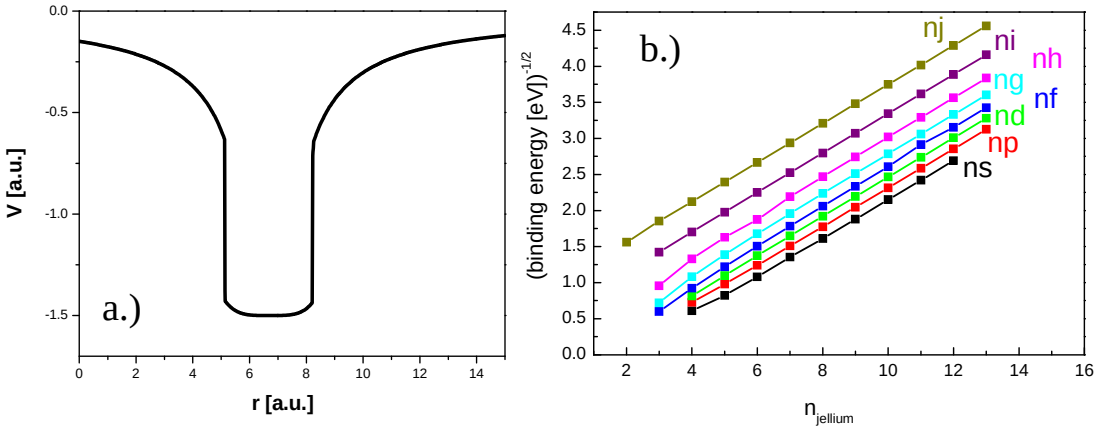

Figure 4.7: *a.) Radial dependence of the jellium potential for C_{60} based on [PNi93]. The defining equation is presented in Eq. 4.4 b.) calculation of binding energies for different angular momentum series.*

To compare the calculated binding energies to experimental data, Lorentzian peak fits were made of the photoelectron spectra for both 800 nm and 400 nm, as shown in Fig. 4.8a) and b). Assignments of the experimental peaks are presented in Table 4.1. The first and second column consist of the Lorentzian-fit peak positions of the binding energies (calculated from the measured kinetic energy) of 800 nm excitation and 400 nm excitation, respectively. The third column assigns the calculated states to the peaks. The fourth column represents the conversion to hydrogenic orbitals. The last column indicates if the peak is strong in the photoelectron spectra. When the peak is strong for only one of the wavelengths, parentheses are used to indicate the wavelength.

A direct comparison of the experimental and calculated values, Fig. 4.9, shows a strong correlation with three particular angular momentum series, ℓ = 3(f), 5(h), and 7(j). These three series resulted in a standard deviation between calculation and experiment of ≤0.02 eV, which is significantly lower than the standard deviation resulting from fits of other series (>0.03 eV). The observed series are consistent with the absorption of an even number of photons from either 800 nm or 400 nm from the

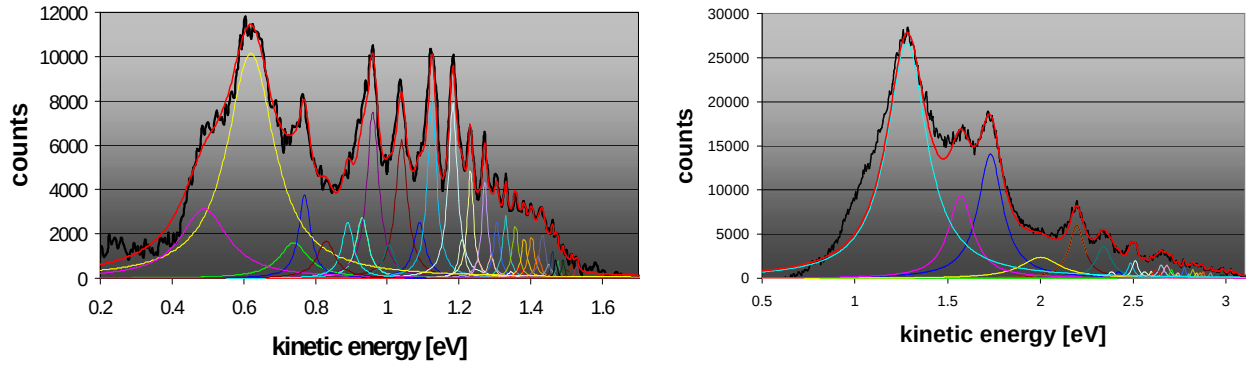

Figure 4.8: *Lorentzian peak fits for a)800 nm spectrum, measured with 1.1*10^{12} W/cm^2 and 1.5 ps pulse duration b) 400 nm spectrum, measured with 4*10^{10} W/cm^2 and 2.1 ps pulse duration. Positions are shown in Table 4.1.*

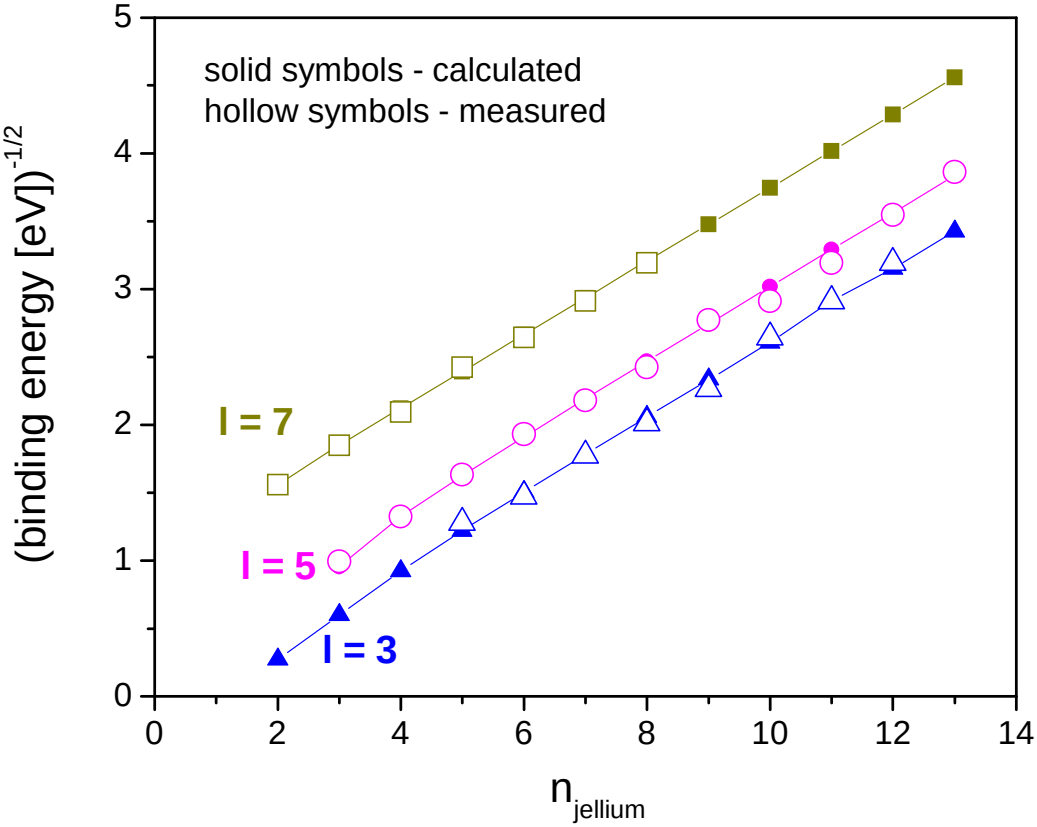

Figure 4.9: *Comparison of calculated binding energies to experimentally fit peak positions. Solid symbols represent calculated binding energies. Open symbols represent the experimental values.*

Table 4.1: *The assignment of experimentally fit peaks are shown in the table below for 800 nm (1.5 ps, 1.1*10^{12} W/cm^2 and 400 nm (2.1 ps, 3*10^{10} W/cm^2). Strong peaks, clearly definable peaks are marked with "*". When the peak is strong for only one wavelength, the strong peak wavelength is indicated in the parentheses. The fit values are the binding energies in eV. The hydrogenic states are calculated by (n, ℓ)=$(n_{jellium} + \ell, \ell)$ with n the principle quantum number.*

800 nm [eV]	400 nm [eV]	Jellium Assignment	Hydrogenic State	Comment
1.010 ± 0.05	1.030 ± 0.05	3h	8h	*
0.880 ± 0.08	0.870 ± 0.03	4g,5p	8g,6p	*
0.760 ± 0.05	...	5d	7d	
0.730 ± 0.02	0.735 ± 0.03	??	??	*
0.670 ± 0.08	...	5f	8f	weak
0.610 ± 0.02	0.630 ± 0.03	6p	7p	*(400 nm)
0.570 ± 0.02	0.570 ± 0.035	4h	9h	*
0.540 ± 0.02	...	6d	8d	
0.495 ± 0.02	...	5g, 3i	9g, 9i	weak
0.460 ± 0.02	0.470 ± 0.035	6f	9f	*
0.410 ± 0.02	0.410 ± 0.03	2j	9j	
0.375 ± 0.015	0.365 ± 0.02	5h	10h	*
0.317 ± 0.015	0.325 ± 0.015	7f	10f	*(800 nm)
0.292 ± 0.01	0.305 ± 0.015	3j	10j	*(400 nm)
0.268 ± 0.01	0.265 ± 0.015	6h	11h	*
0.247 ± 0.01	0.250 ± 0.02	8f	11f	weak
0.228 ± 0.01	...	4j	11j	*(800 nm)
0.210 ± 0.01	0.220 ± 0.015	7h	12h	*(400 nm)
0.195 ± 0.01	0.200 ± 0.015	9f	12f	*
0.170 ± 0.01	0.180 ± 0.015	8h,5j	13h,12j	*
0.155 ± 0.01	...	9g, 7i	13g, 13i	weak
0.143 ± 0.01	0.147 ± 0.015	10f,6j	13f,13j	*(800 nm)
0.130 ± 0.01	0.130 ± 0.015	9h	14h	*(400 nm)
0.118 ± 0.01	0.115 ± 0.015	11f,10h,7j	14f,15h,14j	*
0.098 ± 0.01	0.095 ± 0.015	12f,11h,8j	15f,16h,15j	*
0.080 ± 0.01	...	12h	17h	...
0.067 ± 0.01	...	13h	18h	...

HOMO level of C_{60} , which has an angular momentum of $\ell = 5$. It is possible that 4 photons of 800 nm (or 2 photons of 400 nm) are absorbed as they provide enough electronic energy to reach the highly excited states. Using dipole selection rules ($\ell \pm 1$) for four absorbed photons would result in the observed series. The angular momentum is not expected to change after excitation on short time scales since there is no spin-orbit operator. For these relatively low n Rydberg states, the interaction with the core could be expected to lead to a large deviation from hydrogenic orbitals. Nevertheless, an excellent agreement between theoretically calculated electronic states and experimental values exists.

Quantum Defects

The number of nodes in the radial wavefunction $N = n_{jellium} - 1$ of the jellium model can be converted into the principle quantum number, n, where the number of nodes of the radial wavefunction is given by $N = n - \ell - 1$. Thus the transformation from $n_{jellium}$ to principle quantum number n is given by

$$n = n_{jellium} + \ell \tag{4.5}$$

This has been made for all fit peaks shown in Table 4.1. We can re-plot the experimental data versus the principle quantum number and fit the curves to find the quantum defect of the three series.

The quantum defect for the f, h, and j series are $\delta_f = 4.37 \pm 0.05$, $\delta_h = 5.26 \pm 0.04$, and $\delta_j = 4.22 \pm 0.02$,respectively. The values of the quantum defects seem to have no relation to the typical values associated with different angular momentum series. There is also no decrease in quantum defect with increasing ℓ as is be expected. These discrepancies most likely arise from the assumption of the C_{60} molecule from a point source for low principle quantum numbers, i.e., small radius orbitals.

4.2.3 Excitation Mechanisms: Single Active Electron

Although experimental observation and quantitative analysis of the single pulse measurements leads to identification of the Rydberg states, the question remains: "How are all of these states populated"?

One approach to answer this question would be through a direct population process by multi-photon absorption of one electron. In this model, one or more photons

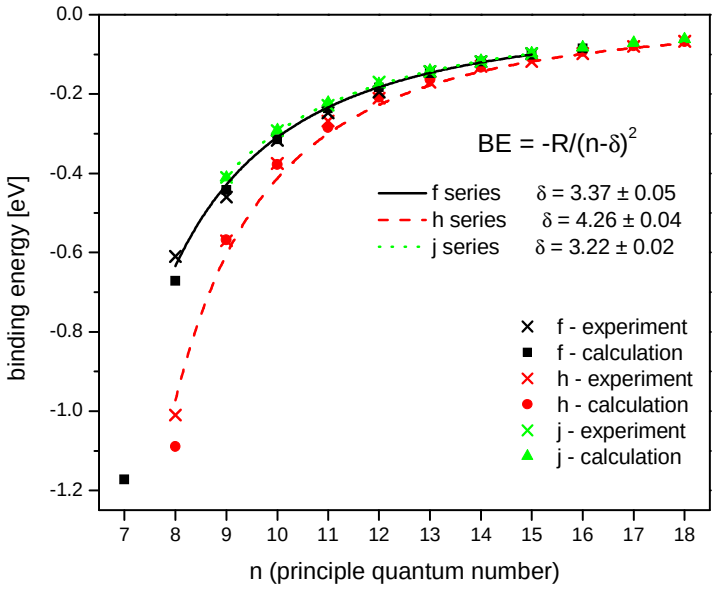

Figure 4.10: *Fit quantum defects of Rydberg series f, h, and j. Here, the number of nodes in the jellium notation has been translated into the principle quantum defect in a hydrogenic picture.*

resonantly excites a highly excited electronic state from a lower lying electronic state, e.g., ground state. The absorption of one or more additional photons provides enough energy to exceed the ionization potential and an electron will be emitted, a resonant enhanced multi-photon ionization (REMPI). Femtosecond, high intensity excitation, allows for resonant multi-photon excitation of Rydberg states as seen for benzene and toluene molecules [WGr83]. The sharpness of the measured peaks and the well defined series may indicate an excitation of a single electron into the well-resolved states. Several effects may allow for excitation of many states within a single laser pulse. The broad spectral bandwidth would allow for resonant excitation of states lying within the bandwidth. The uncertainty principle dictates the energy bandwidth of the incident laser pulse, namely the shorter the pulse the wider the energy bandwidth and greater chance to populate close lying Rydberg states. Additionally, high intensity laser interaction will cause shifts in electronic states into multi-photon resonance (Freeman resonances [FBM87]) or give additional quiver energy to the electron (ponderomotive energy). Given the wide range of laser intensities over the interaction volume, excitation of several states is feasible.

Although, these factors may play a role in the excitation of Rydberg states, they cannot explain a direct electronic excitation as the only population mechanism. The

photoelectron spectrum in Fig. 4.1, for example, shows that the Rydberg states are spread over 1 eV of kinetic energy. Direct electronic population of these states from the ground state is not possible, in this case, since the energy bandwidth of the laser was only 10 meV and the ponderomotive energy, for the intensity used, was 60 meV. The combination of these energy bandwidths do not equal the width of the manifold of Rydberg states.

Since a direct electronic excitation cannot explain population of all of the Rydberg states, it was suggested that the internal vibrational energy is important for the population process [BHS01]. C_{60} contains around 4.4 eV of internal vibrational energy at 770 K, the temperature of the effusive oven. Under the inverse Born-Oppenheimer approximation (IBOA), each vibrational state has a corresponding series of electronic levels. This approximation is valid for high n values, where the ionic core has the possibility to rearrange before the electron recombines. In other words, the electron motion is slow in comparison to nuclear motion. For low n's, a system falls under the Born-Oppenheimer approximation (BOA), where the electronic motion is faster than the reorientation of nuclear coordinates. For intermediate n's, neither the IBOA nor the BOA has an exact separation which implies that states of the same total energy are mixed [RLe98]. This occurs when the orbital period is on the same order as the vibrational period.

This mixing of energy can be visualized as follows: an electron is excited into one of several possible vibronic states of the same energy. The mixing of electronic and vibrational energy occurs only close to the core, so that far from the core the electronic states are well defined. When the electron returns to the core, the electron predominantly transfers energy into the vibrational system, leading to the decay of the Rydberg state. Upon the absorption of an additional photon, the electron is emitted. Assuming a principle quantum number of n = 10 (in the Bohr hydrogenic model and not the jellium model), the radius of an electron would be 5.3 nm (i.e., >10 times the radius of C_{60}). This leads to an orbital period of $\sim$ 150 fs, which is only slightly longer than the longest vibrational period ($H_g(1)$ - 122 fs) and allows for significant energy redistribution in each round trip since the electron-vibrational redistribution proceeds on this time scales. The measured energy bandwidth of the Rydberg states corresponds to lifetimes on the order of hundreds of fs, indicating that the electron orbits at least twice before being emitted.

Four photons of 800 nm, provide 6.2 eV of electronic energy. Molecules with vibrational energy up to 1.4 eV, i.e., the difference from IP 7.6 eV and 6.2 eV of

electronic energy, can access the Rydberg states and then be ionized by one photon within the same laser pulse. Thus, molecules with internal energies greater than 1.4 eV will populate states in the ionization continuum, and contribute to the broad background. In this model, the angular momentum is conserved and can explain the most prominent Rydberg series of ℓ = 3, 5, and 7, the strongest being ℓ=5.

However, this mechanism is now considered unlikely because of the propensity of vibrational-less transitions upon excitation and ionization. Hertel, et al. showed for single photon ionization of free C_{60} the signal begins at the ionization potential [HSV92]. If there was an efficient electronic to vibrational coupling upon excitation, the ionization signal would begin significantly lower than the ionization potential.

Although unlikely, the population process suggested needed to be tested. This spurred two experiments. The first experiment was to separate the excitation and ionization steps by two color pump-probe spectroscopy. The second experiment is to reduce the amount of initial internal vibrational energy. The results of these experiments in addition to the consideration above have changed the interpretation, as will be discussed in the following sections.

4.2.4 Time-resolved pump-probe photoelectron spectroscopy

Two-color time-resolved pump-probe spectroscopy was used to investigate the population mechanism of the observed Rydberg states. By implementing the pump-probe technique, a separation of excitation and ionization (+excitation) is achieved.

The measurements were performed with the setup as shown in Fig. 2.28. The two wavelengths were 800 nm and 400 nm, each of ∼120 fs pulse duration. For the measurements presented in this chapter, the polarizations were perpendicularly oriented with the 800 nm polarization parallel to the TOF axis. This was done to distinguish between electrons emitted from each color, since the electrons are primarily emitted along the laser polarization axis [Hof00]. This was not seen to affect the signal intensity, as is shown in Fig. 4.11.

The plot compares the C_{60}^{+} and Xe^{+} ion pump-probe yields for three different polarizations of the 400 nm pulse: parallel to the 800 nm polarization, oriented at 45 degrees, and perpendicular to the 800 nm polarization. The detection efficiency for ions is equal for all orientations of polarization due to the strong extraction field, thus, the yield reflects the ionization probability of the selected ions. The signal count (y-axis) is plotted as a function of time delay (x-axis). Positive time values imply

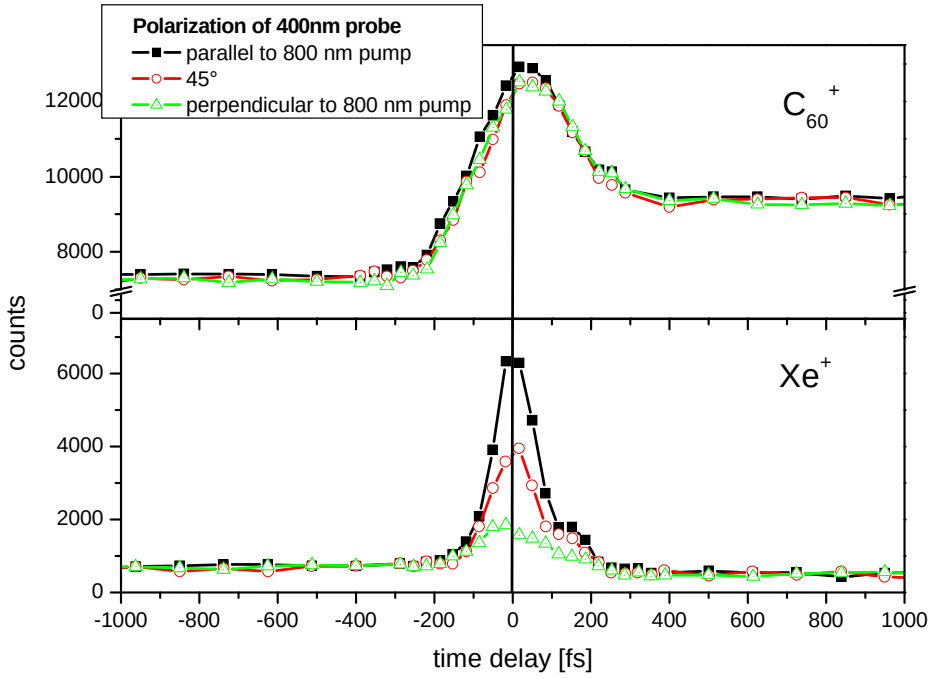

Figure 4.11: *Polarization dependence on C_{60}^+ and Xe^+ yield. Traces recorded with 7*10^{12} W/cm^2 of 800 nm and 3*10^{11} W/cm^2 of 400 nm.*

that the 400 nm pulse interacts with C_{60} before the 800 nm pulse, and vice versa for negative time delays. The Xe^+ yield shows a clear effect of the different laser polarizations. For parallel polarizations, the peak yield is a factor of 3.5 greater than for perpendicular polarizations. The C_{60}^+ yield does not exhibit a dramatic change for different laser polarizations. This can be expected since the redistribution of initial electronic energy takes place on time scales less than 50 fs [CHH00], which is significantly shorter than the pulse duration used in these measurements.

Two graphs are shown in Fig. 4.12. The two contour plots display the measured kinetic energy distribution of electrons versus the time delay between pump and probe pulses. The contour scale is a linear scaling of the intensity of the photoelectron distributions. The photoelectron spectra were measured at 100 fs intervals. The signal is expected to vary smoothly between the points since the C_{60}^+ signal measured with a with smaller step size has a smooth curve (see Fig. 5.19). In addition, the pulse duration would not allow for resolution of features occurring on faster time scales. Each photoelectron spectrum is a sum of 2 million laser shots measured in an electron TOF spectrometer and converted to kinetic energy. Vertical cuts along a particular

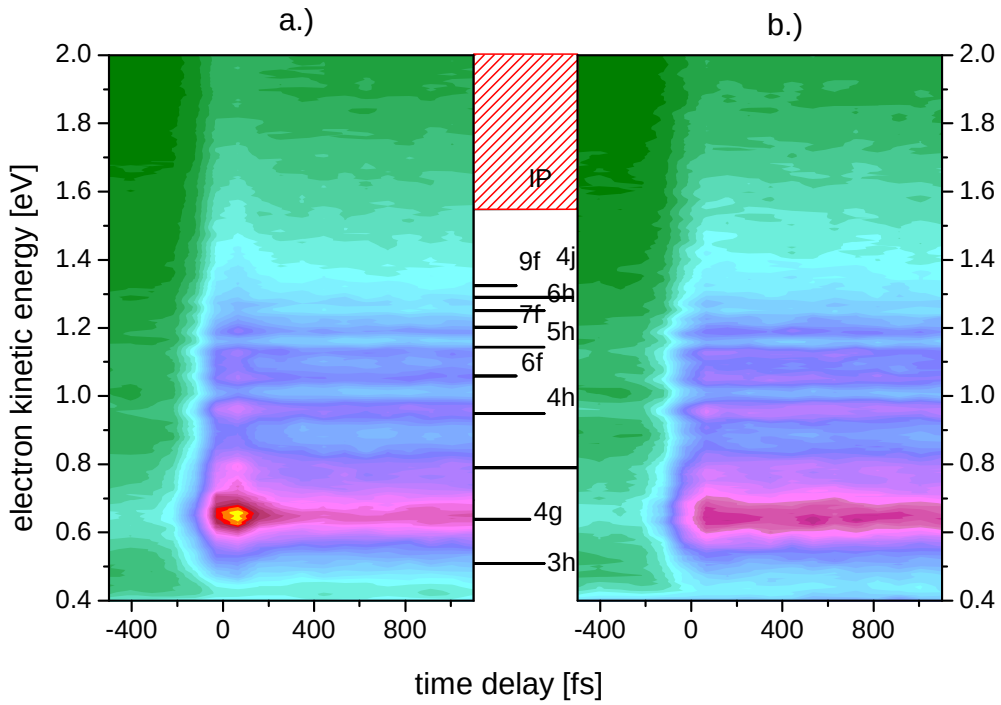

Figure 4.12: *Contour plots of the time resolved pump probe spectra recorded laser intensities of a.) 2*10^{12} W/cm^2 for 800nm and 1*10^{11} W/cm^2 for 400 nm b.) 2*10^{12} W/cm^2 for 800nm and 0.5*10^{11} W/cm^2 for 400 nm. Between the graphs is a line graph indicating the calculated peak positions. The contour is a linear scale.*

time delay give the photoelectron kinetic energy distribution. Horizontal cuts follow the time evolution of a particular state. The 800 nm laser intensity was the same for both measurements at 2*10^{12} W/cm^2. The photoelectron yield was measured at two different intensities of the blue probe pulse: Fig. 4.12 a.) 1*10^{11} W/cm^2 b.) 0.5*10^{11} W/cm^2.

The spectra contain numerous horizontal lines, which are attributed to the Rydberg series and are identified by their nℓ state in the center of Fig. 4.12. The kinetic energy resolution (Δ E $\cong$ 20 meV) does not allow for identification of all peaks listed in Table 4.1, but is comparable to the resolution of the spectrum shown in Fig. 4.5b.

The feature present in both spectra is the increase in photoelectron signal for positive time delays, where the 400 nm pulse leads the 800 nm pulse. This is observed for all kinetic energies.

In Fig. 4.12a), with the higher intensity of 400 nm, a peak is present near zero time delay. This peak is not as prominent in the weaker 400 nm spectrum in Fig. 4.12b).

A horizontal slice along the 4g Rydberg state allows for a closer look into the pump-probe time evolution.

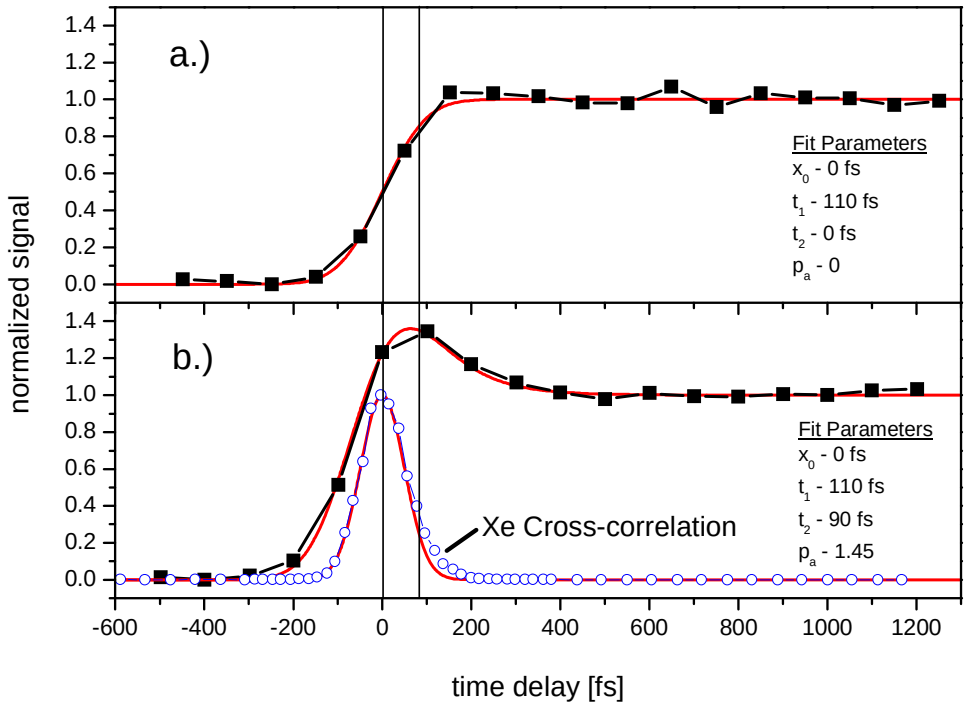

Figure 4.13: *Temporal profile of energy slice taken along the 4g Rydberg state a.) 2*10^{12} W/cm^2 for 800nm and 0.5*10^{11} W/cm^2 for 400nm b.) 2*10^{12} W/cm^2 for 800nm and 1*10^{10} W/cm^2 for 400nm.*

In Fig. 4.13, the normalized amplitude of the 4g Rydberg peak is plotted against the time delay between the two laser pulses. Normalization was made such that the signal for long positive time delays is one. In Fig. 4.13a, the yield resulting from a weaker 400 nm pulse is shown. It has been fit with an error function, which is given by Eq. 4.6. The error function is the integral of a Gaussian pulse and typically indicates the population of a long living excited state.

$$S(t) = 1 + erf((t - t_0)/T_1) \tag{4.6}$$

where T_1 is the cross correlation width of the two pulses which was determined to be 110 fs $\pm$ 20 fs by measurements on xenon and t_0 is the shift with respect to time zero.

Time zero is difficult to determine in situ for photoelectron spectra since similar kinetic energies of electrons resulting from different molecules are indistinguishable.

However, a few assumptions can be made so that an accurate comparison of the two curves is possible.

The "time zero" of Fig. 4.13a) has been set so that at $t_0 \equiv 0$ fs, the signal was 0.5. This adjustment would be justified if the excitation process is incoherent or has multiple near coherent transitions, however, if the excitation is coherent time zero would be set at 0.3 [FRR96]. It was not possible to determine which of these scenarios best reflects the excitation of C_{60}. Therefore, the true "time zero" of this curve is $t_0 = 0 \pm 50$ fs. The experimental data was best fit with the error function of time constant $T_1 = 110$ fs.

The Rydberg state yield measured for an increased intensity of the 400 nm pulse, shown in Fig. 4.13b), contains a peak near zero time delay that is followed by a fast exponential decay. This curve was fit by Eq. 4.7.

$$S(t) = (1 + p_a * exp(-((t - t_0)/T_2))) * (1 + erf((t - t_0)/T_1))/2 \qquad (4.7)$$

where T_1 and t_0 have the same definition as in Eq. 4.6, T_2 is the time constant of the exponential decay, and p_a is the amplitude. The exponential decay describes the decay of the initially excited electronic states. The signal in Eq. 4.7 is approximately a convolution between Eq. 4.6 and an exponential decay.

The parameters resulting from the fit of the weaker 400 nm intensity must be consistent for this fit, thus $T_1 = 110$ fs $\pm$ 20 fs and $t_0 = 0$ fs (defined). This essentially fixes the peak position of the fit curve. This leaves two remaining fit parameters, which were empirically found to be $T_2 = 100$ fs $\pm$ 20 fs and $p_a = 1.5 \pm 0.2$. The peak position is located at +80 fs with respect to the defined time zero.

A second check of the temporal position can be made. If the xenon cross-correlation also defines time zero (which is true with no intermediate resonances), the difference between the xenon peak and C_{60}^+ peak is in good agreement with the separation measured in two color pump-probe ion spectroscopy (see Fig. 5.19), in which the two yields were measured simultaneously. This gives added confidence for the definition of the relative time zero.

No detectable decay of the signal for positive time delays is observed on the 1 ps time scale. On an extended time scale, up to 7 ps, a slight decay of the signal is detected, as shown in Fig. 4.14. The decay is strongest in the case of the 4g Rydberg state. To quantitatively analyze these decays, a further exponential decay was added

to the fit function, as shown in Eq. 4.8.

$$S(t) = (1+p_b*exp(-((t-t_0)/T_3)))*(1+p_a*exp(-((t-t_0)/T_2)))*(1+erf((t-t_0)/T_1))/2 \quad (4.8)$$

where p_b is the amplitude and T_3 is the time constant for long (ps) delays. In Fig. 4.14, the experimentally measured signal for several different Rydberg states are compared to three different time constants, T_3 = 10 ps, 100 ps, and 1 ns. The amplitude p_b was 1.2 for the 10 ps decay and 1.05 for the 100 ps and 1 ns decays. The change of amplitude was done to best match the signal height at 500 fs delay.

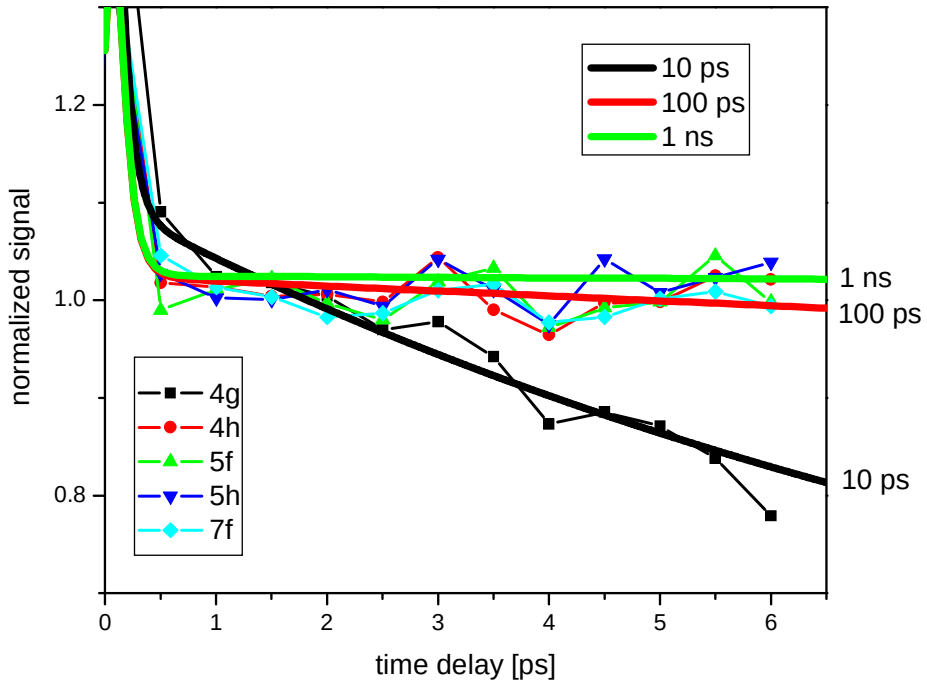

Figure 4.14: *Energy slice taken along several Rydberg state, from laser intensities of 2*10^{12} W/cm^2 for 800nm and 1*10^{10} W/cm^2 for 400nm. The signal is compared to different decay times of 10 ps, 100 ps, and 1 ns.*

Although 7 ps time delay was not enough to accurately determine the time constant of the decay, a lower bound can be determined (assuming no further dynamics occur beyond the exponential decay). A lower bound for the time constant of 100 ps is determined for the 4h, 5f, 5h, and 7f Rydberg state. Before a discussion of the population mechanisms and their decays, results concerning the influence of internal energy will be presented.

4.2.5 Internal Energy Dependence on the excitation of Rydberg States

In this section, photoelectron yields resulting from C_{60} containing two different internal energies are compared. The apparatus providing the cold molecular beam has been described in Chapter 2. Photoelectron spectra were measured for both sources without changing the experimental laser parameters (λ = 800 nm, 2.5*10^{12} W/cm^2, 100 fs) or the vacuum conditions. At this laser intensity, little to no fragmentation of C_{60} is observed from either source.

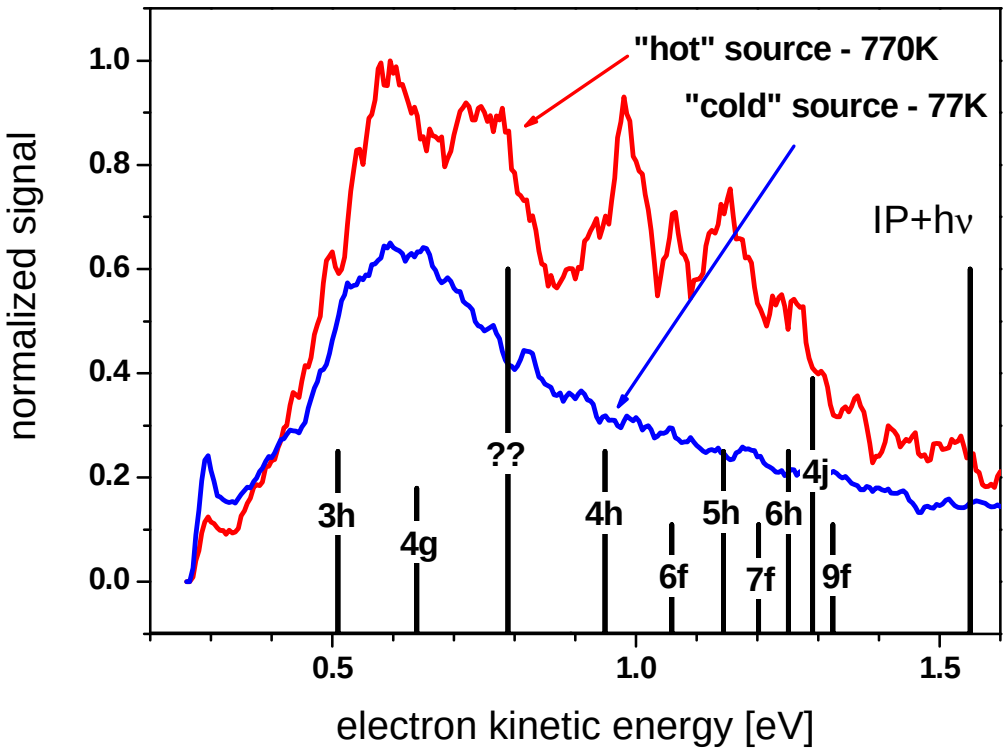

Figure 4.15: *Comparison of hot (770 K) and cold (77 K) sources. Both spectra were recorded with a wavelength of 800 nm, a pulse duration of 100 fs, and an intensity of 2.5*10^{12} W/cm^2. The assigned Rydberg states are shown with the stick figure. The height of the sticks* ***does not*** *represent their strength. One peak has not been identified and labelled with "??".*

The measured photoelectron spectra are shown in Fig. 4.15. The spectra have been normalized to each other for electron kinetic energy greater than 2 eV, i.e., the thermal tail, which is expected to be the same. The spectrum measured with

770 K C_{60} clearly displays the Rydberg peaks, although the spectrum resolution and signal-to-noise ratio is reduced. Plotted below the spectra are the calculated peak positions. The peak structure is in reasonable agreement with the calculated values. In contrast, in the photoelectron spectrum measured with vibrationally cold, 77 K C_{60} no Rydberg states can be identified. Unfortunately, no spectra were obtained between these temperatures due to experimental limitations.

It is apparent that the internal energy plays a key role in the population of the Rydberg states, most likely either by enhancing the Franck-Condon overlap for the excitation of an electron to an excited state or by mediating the vibronic coupling. The interpretation of the influence of the internal temperature will be discussed in more detail in the following section.

4.2.6 Excitation Mechanisms : Multiple Active Electrons

The two color pump-probe measurements give new insight into the population mechanism and dynamics, which has subsequently led to new possibilities for the interpretation of the population mechanism. In this new interpretation, the single active electron picture of C_{60} excitation is dropped in favor of multiply active electrons (MAE). There are at least three possible ways which MAE can aid in excitation of Rydberg states. Superexcited states as proposed by Schick et al. [SWe01a] for phenol, "nonadiabatic multielectron dynamics" (NMED) as first proposed by [LBR01] for extended π-orbital systems, or multiple active electron exciation into the LUMO+1 band followed by an efficient energy mixing.

A super-excited molecular state occurs when an electronic valence orbital lies energetically above the ionization potential. This can occur through the excitation of two electrons into two valence orbitals. Excitation of Rydberg states via super-excited states has been suggested recently for phenol [SWe01a]. In their work, excitation of the superexcited state was achieved by two photon excitation in the singlet manifold to state S_n, followed by electronic to vibrational energy relaxation along isoenergetic vibronic levels of the neutral molecule. Ionization was achieved by single photon ionization from these vibrationally hot Rydberg states.

Yasumatsu et al. have observed a superexcited state in C_{60} at 9.3 eV [YKK96], measured with single photon excitation, which would be resonant with 6 photons of 800 nm (or 3 photons of 400 nm). The lifetime of this superexcited state was found to be on the order of 1 ps. The excitation of this superexcited state with 800 nm laser

radiation should be strongly intensity dependent since it corresponds to a direct 6 photon process. The intensity dependence of the photoelectron spectra do not clarify this non-linear process [BHS02]. Furthermore, at the intensities needed to excite the super-excited state via a multi-photon process, the excitation of multiple electrons is likely [ZSG03].

Recently, a new non-resonant strong field ionization mechanism has been proposed for polyatomic molecules [LBR01][LBI02][MSR03][MRS04]. In this model, the adiabatic approximation is expected to fail for large molecules, especially for those with delocalized electron orbitals, because the electronic motion is no longer short in comparison to the laser period, in other words, the electron may not be able to adiabatically follow the electric field. Secondly, doubly excited states exist below the ionization threshold, implying that the SAE picture is no longer valid. This can also occur in the classical (atomic) tunneling picture where the Keldysh parameter, $\gamma < 1$. [LBR01]. "Non-adiabatic" is, in this model, defined as the relation of the electrons' driven motion to the electric field oscillations. This is different from a typical non-adiabatic coupling between electronic and vibrational motions.

Excitation of multiple active electrons have been interpreted for polyatomic molecular systems in strong laser fields, such as conjugated hydrocarbon chains [LBI02] and polyaromatic molecules [MSR03][MRS04]. For these extended π-systems a "non-adiabatic multielectron dynamic" (NMED) model was developed to explain energy absorption of the molecule [LBR01][LBI02].

In this model, Landau-Zener type non-adiabatic transitions occur generating a quasi-continuum. The departure from the adiabatic regime arises due to a rapidly oscillating electric field and/or increasing Stark shift. As a quantitative estimation, the probability of a Landau-Zener transition during half a laser cycle can be estimated by Eq. 4.9 [LBI02].

$$P_{LZ} \sim e^{-\pi\Delta_0^2/4\hbar\omega_L\varepsilon\mu} \tag{4.9}$$

where Δ_0 is the field free energy level spacing, μ is the dipole matrix element, ω_L is the laser frequency, and ε is the electric field strength. The authors define the situation where non-adiabatic transitions become important as $\Delta_0^2 = \hbar\omega_L\ q\ \varepsilon\ L$, where L is the "length" of the molecular system. The process becomes more important as the length increases, the laser frequency increases, and/or the electric field amplitude increases.

C_{60} similarly contains delocalized π-orbitals, and thus is a candidate to exhibit NMED under the right laser excitation conditions. C_{60} has 60 π electrons, which

lie near the Fermi level and play an important role in determining the electronic structure [DDE96]. A simple calculation of the onset intensity of "NMED" for 800 nm and 400 nm, using length, L = 10 $\AA$ (cage diameter) and Δ_0 = 3 eV (HOMO->LUMO+1 gap), shows that the corresponding intensities are 4.5*10^{12} W/cm^2 and 1.1*10^{12} W/cm^2, respectively.

Under these simple approximations, "*non-adiabatic multi-electron dynamics*" are not expected to be the dominate mechanism to populate Rydberg states in C_{60} since the series is clearly excited even for intensities lower than the calculated onset. In addition, the NMED model is entirely independent of the vibrational content of poly-atomic models, as the mixing of energy occurs in the electronic system, i.e., the quasi-continuum. The internal energy dependence of Rydberg excitation would be consistent with the NMED model only if vibrational energy was needed to populate the LUMO+1 "doorway state". Internal vibrational energy may indeed influence the excitation of the doorway state by improving the Franck-Condon overlap or, for the two-photon 800 nm transition, inducing a Jahn-Teller distortion leading to Renner-Teller allowed transitions. Further experiments are needed here to better define a possible "doorway state".

Although the definition of "NMED" presented by [LBI02] is not consistent with the experimental results for excitation of the Rydberg series for low intensities, multiple active electrons may still be the mechanism of excitation. Theoretical simulations using time dependent density functional theory [TNE01, BCM01, Bau04] and matrix formalism [ZSG03] for isolated C_{60} reveal that excitation of multiple electrons occurs even for moderate laser intensities of 0.3*10^{11} W/cm^2, which is slightly lower than the weakest intensities used to excite C_{60} in the two-color pump-probe measurements.

Zhang, et al. [ZSG03] show for 10 fs laser pulses, 0.3*10^{11} W/cm^2, and HOMO->LUMO+1 resonant photons, 2 electrons are transfered to the LUMO+1 excited states. Excitation occurs to antibonding electron orbitals which creates a new equilibrium radius. The cage then begins to expand and oscillate about the new equillibrium with the frequency of oscillation corresponds to the totally symmetric breathing mode, $A_g(1)$. The oscillation about the new equilibrium can be interpreted as an oscillation of the potential energy. Since the total energy remains constant, i.e., no electron emission, fragmentation, fluorescence, etc. , the energy must oscillate between the electronic and potential energy. The oscillation covers $\sim$ 2 eV, which shared with the two excited electrons means each electron oscillates with an amplitude of 1 eV in the LUMO+1 band.

In relation to the present experimental result, this oscillation between nuclear and electronic degrees of freedom provides the energy spread required to populate the Rydberg states from the LUMO+1 band and proceeds via a one electron, multi-photon process. The exchange of energy can occur through efficient non-adiabatic transitions.

The two-color pump-probe measurements show the time dynamics of Rydberg state excitation. The increase in photoelectron yield for positive time values is likely to be initiated by a near resonant absorption of 400 nm photons corresponding to the HOMO -> LUMO+1 transition. Haufler, et al. [HCC91], using resonant enhanced two photon ionization (R2PI) on cold molecular beams, found two absorption peaks near 400 nm and coincide with the present measurements. The signal of the Rydberg peaks appears to decay on a >100 ps time scale, the decay of these signal may indicate the lifetime of the doorway" state. No measurements exist concerning the lifetime of the LUMO or LUMO+1 electronic states of isolated C_{60}. In thin films, the lowest lying electronic state (LUMO) has been found to have a lifetime of 130 $\pm$ 30 ps [JKE97][LDE01]. LUMO+1 was found to be 300 fs $\pm$ 30. Stepanov, et al. [SPS02] have studied isolated C_{60} in rare gas matrices and found similar time constants. However, for molecules in the gas phase, the lifetimes are often significantly longer since there is no intermolecular interaction.

Near time overlap of the two pulses, the signal is influenced by the intensity of the 400 nm pulse. For the pump-probe spectra with 400 nm pulse of intensity $0.5*10^{11}$ W/cm^2, the Rydberg signal is modelled by the error function to describe the population of the LUMO+1 band. As the blue intensity is increased to $1*10^{11}$ W/cm^2, an additional peak appears near the overlap of the two pulses. The additional maximum for higher intensity 400 nm pulse with higher intensity can arise from multiple excitation followed by a rapid electron thermalization (el-el scattering) in the LUMO+1 band. The decay time here is on the order of the laser pulse duration.

In conclusion, the signal of Rydberg states, as the two-color pump-probe measurements point out, is enhanced with an excitation of an intermediate state. The enhanced absorption of 400 nm reveals that one possible intermediate state is the LUMO+1. From this excited state, broadened by non-adiabatic transitions, an electron can be excited to the Rydberg states and be emitted by a lower order process (minimum 3) as compared to the minimum 5 order process found on negative time scales. As the intensity is increased, nonlinear excitation of the C_{60} molecule increases, while the two pulses overlap.

Unfortunately, the internal energy dependence cannot be directly tied to the pump-probe measurements in the MAE picture. It is however clear that internal energy plays a major role for 800 nm laser excitation. This can be explained by the importance of the doorway state, which is dipole forbidden for 800 nm. The additional of internal vibrational energy may allow for a electronic dipole forbidden transition to be allowed, i.e., a Jahn-Teller distortion.

For a large and complex system such as C_{60}, it is remarkable that well defined electronic states can be measured in strong laser fields. Although detected and identified, one definitive excitation mechanism may be impossible to deduce due to the electronic and vibrational complexity. Based on the present information, a multiactive electron picture is the most probable explanation for the excitation of Rydberg states. Theoretical work [TNE01][BCM01][ZSG03] give confidence that multiple electron excitation is possible for C_{60} under the experimental laser conditions used in this work and its importance for energy absorption in C_{60}.

4.2.7 Angular Resolved Photoelectrons

In this section, experimental results concerning the angular distribution of electron emission from C_{60} is presented. Particular focus is given to the electrons coincident with C_{60}^{+} that have kinetic energies corresponding to Rydberg states. A detailed quantitative analysis is not made, as the complexity of the system and photoelectron angular distributions (PAD) are prohibitively difficult.

The angular resolved electron emission of different ATI peaks of photoelectron spectra of C_{60} has been measured previously [Hof00]. By rotating the laser polarization axis with respect to the electron TOF axis, the angular emission of electrons was mapped. This was done for 800 nm, 30 fs, $5*10^{13}$ W/cm^2 laser excitation, as well as 400 nm, 50 fs, $6.9*10^{12}$ W/cm^2. However, in these experiments, the coincidence technique was not possible, thus no correlation to emitting species (background atoms or molecules and higher charge states of C_{60}) could be made.

In the present experiment, the photo-electron photo-ion coincidence (PEPICO) technique was applied to measure the angular distribution of electron emission from C_{60}^{+} and C_{60}^{2+} . All spectra were taken with a single laser pulse of duration 30 fs. Three laser intensities were used, $5*10^{13}$ W/cm^2, $1*10^{14}$ W/cm^2, and $2*10^{14}$ W/cm^2. The finest electron kinetic energy resolution achieved was 0.27 eV. A brief description of the apparatus is presented in Chapter 2. The laser polarization is oriented along

the 0 - 180° line where 180° indicates the direction of the detector. The spectra were measured only between 0 and 180 degrees. The points at 2°, 6°, and 10 ° (and also 178°, 174°, and 170°) were removed because their statistical error was too large. Since the spectra must be symmetric around the laser polarization axis, they can be mirrored over the laser polarization axis for visualization purposes. Additionally, the spectra are symmetric about the 90 - 270° axis since the laser polarization is an axial vector.

The measured spectra are expected to show this symmetry for single charge only, in this case, differences observed are attributed to experimental artifacts. For higher charge states, since only one electron is recorded, there is a difference in the probability of detection of electrons emitted in the "forward" direction and that in the "reverse" direction, leading to a measurement asymmetry.

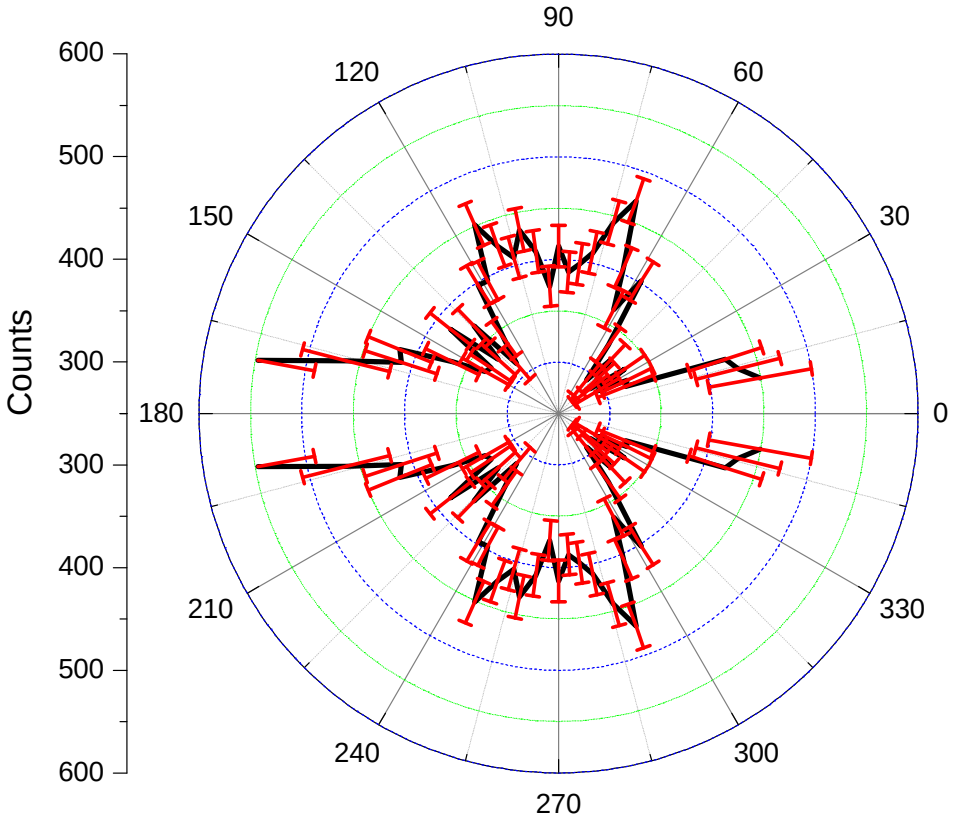

Figure 4.16: *Angular resolved photoelectron spectrum in coincidence with* C_{60}^{+} *. The spectrum was recorded with a wavelength of 800 nm, a pulse duration of 30 fs, and an intensity of* $5*10^{13}$ W/cm^2*. This spectrum consists of electrons of kinetic energy between 0.8 and 1.1 eV as indicated by the box in Fig. 4.17. The angle denotes the polar angle with respect to the laser polarization.*

The polar plot in Fig. 4.16 shows the electron signal for kinetic energies of photoelectrons between 0.8 and 1.1 eV correlated to C_{60}^{+} versus emission angle with respect to the laser polarization axis. The spectrum was recorded with 0.5° resolution, in the analysis this was reduced to 4 ° (by summing the signal in 8 * 0.5°-bins) to improve the signal-to-noise ratio. Error bars indicate the statistical counting error.

Two prominent side lobes oriented at $\sim 70°$ and $\sim 110°$ with respect to the laser polarization axis are seen. The spectrum is comparable to the S = 0 spectrum of Hoffmann [Hof00]. In the present measurements, the relative height of these peaks are more prominent than found in [Hof00]. One cause for this discrepancy is that the spectrum in Fig. 4.16 consists of a smaller energy range where the side lobes are at a maximum, as is observed in Fig. 4.17.

The interpretation of these spectra require looking at the scattering of partial electronic waves from the ionic core. The resulting spectrum is a consequence of constructive and destructive interference of the partial waves. The photoelectron angular distributions can be quantitatively analyzed through the sum of even Legendre polynomials, or more generally (Eq. 4.10), a superposition of spherical harmonic waves [Rei03].

$$\psi_e = \sum_{lm} c_{lm} e^{i\delta_l} Y_{lm}(\theta, \phi) \tag{4.10}$$

where c_{lm} are coefficients containing information about the radial and angular components, δ_l is a scattering induced phase shift, and $Y_{lm}(\theta,\phi)$ are the spherical harmonic functions. For molecular systems, ℓ is no longer a good quantum number and more than two partial waves are necessary to describe a particular electronic wavefunction.

Although the multiphoton and MAE excitation processes are expected to severely complicate understanding of these plots, the presumed single photon ionization from Rydberg states may allow for a quantitative analysis to be made in future theoretical works, as has been shown for Argon [CHW03].

A few further observations can be made from the present experiments. A comparison of the electron angular distribution for different electron kinetic energies between 0 and 2.72 eV is shown in Fig. 4.17. The contour plot shows 10 energy regions of 0.27 eV width versus angle with 4° angular resolution. A horizontal slice results in a polar plot similar to Fig. 4.16.

The contour plot shows, in addition to strong peaks along the laser polarization axis, two peaks at $\sim 70°$ and 110°. These peaks are most prominent between 0.54 and

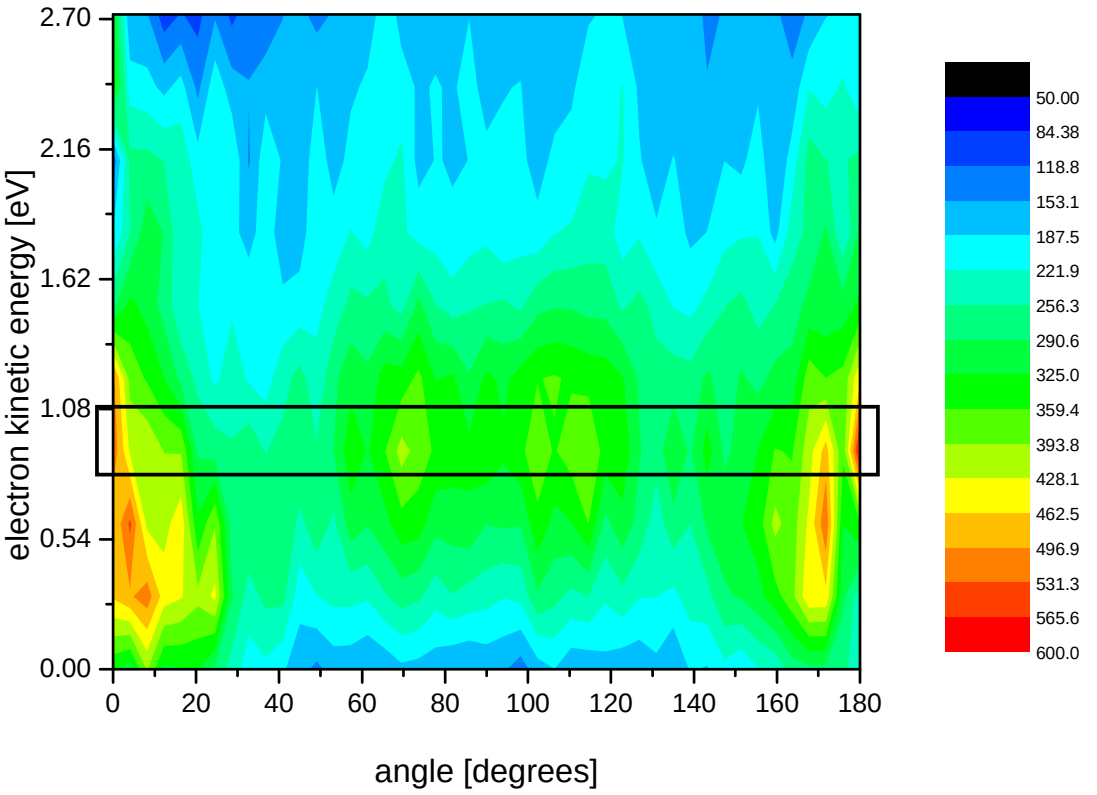

Figure 4.17: *Angular resolved photoelectron spectrum in coincidence with* C_{60}^{+} *. The spectrum was recorded with a wavelength of 800 nm, a pulse duration of 30 fs, and an intensity of* $5*10^{13}$ W/cm^2*. The angle denotes the polar angle with respect to the laser polarization.*

1.35 eV. This energy corresponds to several of the strongest of the Rydberg peaks as observed in Fig. 4.1. It should be noted that the energy resolution of the laser used was 85 meV, which does not allow for individual resolution of any of the Rydberg states. Photoelectron spectra measured under similar laser conditions but smaller angular acceptance Fig. 4.5c, show two broad peaks with peak positions of $\sim$ 0.5 eV and $\sim$1.0 eV. The angular acceptance for this spectrum was less than 1°. Since the experimental results of the present measurement are not reliable in this region, a comparison cannot be made.

An intensity dependence of the coincident C_{60}^{+} electrons is shown in Fig. 4.18. The plot shows the normalized electron signal versus angle with respect to the laser polarization axis. The signal is normalized with respect to the total electron signal coincident with C_{60}^{+} .

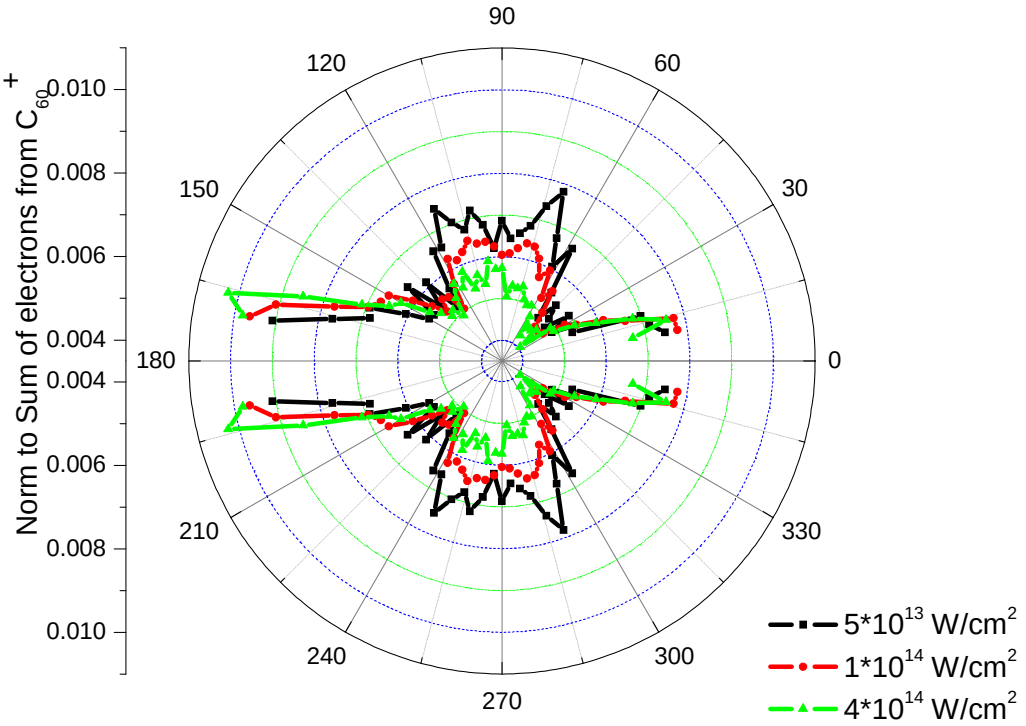

Figure 4.18: *Comparison of angular resolved photoelectron spectrum in coincidence with C_{60}^{+} for three different intensities, 5*10^{13} W/cm^2, 1*10^{14} W/cm^2, and 2*10^{14} W/cm^2. The kinetic energy range of the photoelectrons was between 0.8 and 1.1 eV, as indicated in Fig. 4.17. The angle denotes the polar angle with respect to the laser polarization.*

As the laser intensity is increased, the electron emission perpendicular to the laser polarization becomes less pronounced. If we convert these intensities to Keldysh parameters, as prescribed in Chapter 3, we find $\gamma = 1.1$, 0.8, and 0.4, for increasing intensity. For atoms, this marks a change in ionization regimes from the MPI to BSI (barrier suppression ionization).

Finally, the same analysis has been made for electrons coincident with C_{60}^{2+} . The angular distribution of electrons with kinetic energy between 0.816 eV and 1.088 eV coincident with C_{60}^{2+} are shown for three different intensities. The side lobes are still present for the lowest intensity although they are not as prominent as for electrons coincident with C_{60}^{+} .

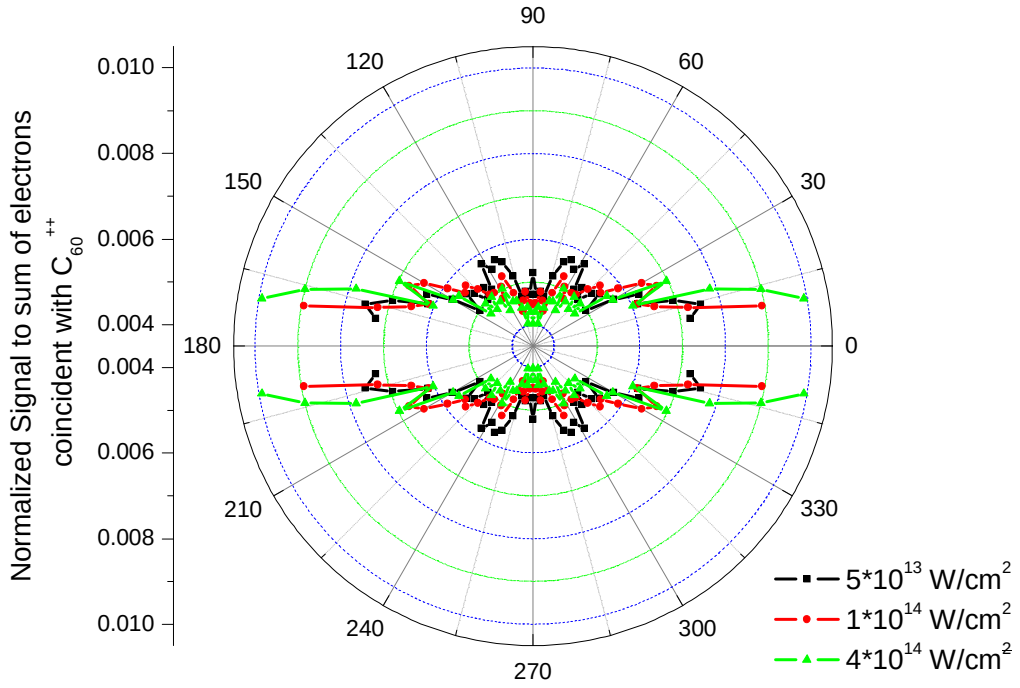

Figure 4.19: *Comparison of angular resolved photoelectron spectrum in coincidence with C_{60}^{2+} for three different intensities, 5*10^{13} W/cm^2, 1*10^{14} W/cm^2, and 2*10^{14} W/cm^2. The kinetic energy range of the photoelectrons was between 0.8 and 1.1 eV. The angle denotes the polar angle with respect to the laser polarization.*

4.3 Summary and Conclusions

Investigation of the peak structure observed in C_{60} photoelectron spectra through single pulse fs-laser excitation has shown that the structure can be identified as Rydberg states. The identification of $n\ell$-states has been achieved by quantitative analysis. Two-color pump-probe spectroscopy and the influence of the internal energy have been studied to understand the population mechanism. Strong evidence indicates the excitation is due to multi-electron excitation of a doorway" state(s) from which a single electron undergoes resonant multi-photon excitation of the Rydberg states, followed by single photon ionization. However, it should be noted that other mechanisms, such as the single active electron model in Section 4.2.3, cannot be completely ruled out based on the data set available.

Several questions have arisen or remain open. Why do we see these particular states? What role does the internal energy play for population of doorway state or population of Rydberg states? What lifetimes do the states have?

Several further experiments can be envisaged to aid understanding of the population process, leading perhaps to a definitive answer. A pump-probe measurement with a 4th harmonic probe would allow for a 1 photon ionization from any excited electronic state. Further internal energy dependence measurements might illuminate the role that vibrations play in excitation of the Rydberg states. Further wavelength dependence of the pump, would provide a more direct evidence of doorway state(s).

The angular resolved photoelectron spectra build upon the experimental database started in [Hof00] and provide motivation for further experiments planned with a new apparatus under construction. Furthermore, theoretical work is beginning to quantitatively understand these complicated patterns.